and the liquid water content aloft is back up to 0.1 g m^{-3}. These calculations thus both illustrate the important influence of turbulence in a fog and indicate why warm-fog seeding is not very effective.

Seeding of supercooled or "cold" fogs is found to be more effective. The idea is to glaciate the fog by introducing dry ice or some heterogeneous freezing nuclei to convert some of the drops to ice particles, which grow rapidly at the expense of the drops because the ice saturation vapor pressure is lower than that of liquid water.[115] The lowered concentration of small drops again means improved visibility. In this case though, once a region of the fog becomes glaciated, it remains clear for a longer time, since any liquid drops mixed into the glaciated region either quickly freeze through contact with the ice particles or evaporate as the ice particles, growing by vapor diffusion, lower the vapor content of the air to a state of subsaturation with respect to liquid water. Eventually, though, the ice particles, like the large solution drops considered above, settle out, and the hole can then fill back in by turbulent mixing of small drops into the clear region, just as in the warm-fog case.

5.1.3 Radiation Fog

The time scale involved in the fog modification problem discussed in the preceding section is ∼1/2 h. Another important problem is the forecasting of fog on a time scale of 12–24 h. As in other types of weather forecasting, a numerical prediction of fog is based on an appropriate form of the fluid dynamical equations, in which the conservation equations for momentum (Newton's second law of motion) and heat (First Law of Thermodynamics) play the central role. We will consider here the forecasting of radiation fog, which is the simplest form of fog. In this case, the momentum conservation is simplified considerably by the fact that the wind is, to a first approximation, calm. Advection fogs involve stronger winds and thereby the effects of advection as well as radiation on the temperature of the air. However, the wind is never completely calm, even in radiation fog, and the slight turbulence present is very important.

The physical parameters of the problem are illustrated schematically in Fig. 5.2. They include the radiative cooling of the earth's surface and the eddy flux of sensible heat $\mathcal{F}_\theta$ [defined by the left-hand equality in (2.188)], which is predominantly downward owing to the strong surface cooling. Since the boundary layer is very stable as a result of the cooling, the buoyancy generation term $\mathcal{B}$ in the turbulent kinetic energy (2.86) acts to suppress turbulence. The only way that turbulent kinetic energy can be generated is through term $\mathcal{C}$, which represents the conversion of mean-flow kinetic energy to eddy kinetic energy by means of the eddy momentum fluxes. Therefore, the mean flow, represented by the wind profile

---

[115] The same process apparently produces holes in clouds when they are seeded naturally by a streamer of ice particles falling from a higher cloud or by aircraft-produced ice particles. For an amusing discussion of these phenomena, see "Holes in clouds: A case of scientific amnesia" by Hobbs (1985).
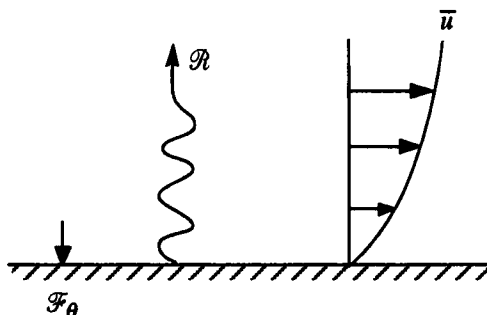
Figure 5.2 Physical parameters of the physics of radiation fog: the net upward radiative heat flux $\mathcal{R}$, which is dominated by infrared and is strongly upward at the ground; the eddy flux of sensible heat $\mathcal{F}_\theta$, which is predominantly downward owing to the strong surface cooling; and the profile of mean wind $\bar{u}$.

in Fig. 5.2, must be specified or predicted in the fog forecasting problem to determine the amount of turbulent mixing that occurs.

The magnitude of the wind at and just above the top of the stable boundary layer may be quite small (e.g., 2–3 m s^{-1}). Nevertheless, it is strong enough to generate turbulent mixing of a magnitude sufficient to be of importance to fog formation, evolution, and dissipation. The form of the momentum equation appropriate for predicting the wind in the planetary boundary layer in a situation of radiation fog is based on the mean-variable equation of motion (2.83). It is assumed that the mean vertical motion is zero. Hence, only the horizontal component of (2.83) is predictive. We further assume that the flow is Boussinesq [i.e., the density term ρ_o disappears from (2.84)], that the mean horizontal wind is so weak that horizontal advection is negligible, and that the horizontal pressure gradient is constant throughout the boundary layer. Then, the horizontal component of the equation of motion (2.83) becomes

$$\frac{\partial \bar{\mathbf{v}}_H}{\partial t} = -f\mathbf{k} \times \left(\bar{\mathbf{v}}_H - \mathbf{v}_g \right) + \bar{\mathcal{F}}_H \qquad (5.2)$$

where the horizontal pressure gradient has been expressed in terms of its corresponding geostrophic wind $\mathbf{v}_g$ [recall (2.22)], and the subscript H indicates a horizontal component of a vector. As indicated in Sec. 2.10, $\bar{\mathcal{F}}_H$ can be formulated with varying degrees of sophistication. Here we use the K-theory formulation, which serves to illustrate the physics of fog formation with a minimum of mathematical complexity, and we assume that on the time scales of interest to forecasting ($\sim$10 h), the vertical mixing dominates over horizontal mixing. Then, according to (2.84), (2.186), and (2.187), the frictional stresses are given by

$$\bar{\mathcal{F}}_H = -\frac{\partial}{\partial z}\left(-K_m \frac{\partial \bar{\mathbf{v}}_H}{\partial z} \right) \qquad (5.3)$$

The mixing coefficient K_m is inversely related to the Richardson number, Ri [defined in (2.170)]. Radiative cooling near the ground produces a temperature

inversion and correspondingly high values of Ri, and mixing is confined to a shallow surface layer. After a fog layer becomes established in an inversion layer, radiation drives the lapse rate back toward a less stable configuration, Ri decreases, and the mixing coefficient is increased to allow more mixing.

While radiative cooling of the ground ultimately drives the radiation fog's formation, it is the delicate *im*balance of the radiation, turbulent mixing of the heat, and phase changes of water that determine the thermodynamic history of the fog, including its formation, evolution, and dissipation. It is important, therefore, to have an accurate and appropriate form of the thermodynamic equation to predict the radiation fog. The essential processes are incorporated in the mean-variable form of the First Law of Thermodynamics (2.78). If we assume for simplicity that the fog consists entirely of liquid drops (i.e., no ice), then with all the assumptions we have made about the air motions, (2.78) may be written as

$$\frac{\partial \bar{\theta}}{\partial t} = \frac{LC}{c_p \bar{\bar{\Pi}}} - \frac{\partial \mathfrak{R}}{\partial z} - \frac{1}{\rho_o c_p} \frac{\partial \mathfrak{F}_\theta}{\partial z} \tag{5.4}$$

where the latent heating term has been written as in (2.13), with C standing for the net condensation (in units of kg of water per kg of air per second), and $\mathfrak{R}$ is the net radiative heat flux (positive upward). The density term in (2.78) does not appear because we are using the Boussinesq version of the relation. Since we are expressing all of the turbulent fluxes by K-theory, $\mathfrak{F}_\theta$ is given by the right-hand side of (2.188). Thus, the eddy flux convergence in (5.4) varies with the mixing coefficient K_θ according to

$$\frac{\partial \mathfrak{F}_\theta}{\partial z} = c_p \frac{\partial}{\partial z}\left(-K_\theta \frac{\partial \bar{\theta}}{\partial z}\right) \tag{5.5}$$

In order to calculate the heat sources associated with condensation and radiation correctly, one must keep track of the amounts of water in the form of vapor and liquid. Hence, an appropriate set of the mean-variable water-continuity equations (2.81) is required. Under the present assumptions, this set may be written as

$$\frac{\partial \bar{q}_v}{\partial t} = -C - \frac{\partial}{\partial z}\left(-K_v \frac{\partial \bar{q}_v}{\partial z}\right) \tag{5.6}$$

$$\frac{\partial \bar{q}_i}{\partial t} = S_i - \frac{\partial}{\partial z}\left(-K_i \frac{\partial \bar{q}_i}{\partial z}\right), \quad i = 1, \ldots, k \tag{5.7}$$

where k is the total number of size categories of water drops considered. The eddy flux of water vapor in (5.6) is expressed by K-theory according to (2.189), and the eddy flux of hydrometeors is expressed by an analogous term in (5.7). S_i represents the microphysical sources and sinks of hydrometeors.

To illustrate the forecasting of the timing of the formation, evolution, and dissipation of radiation fog on a time scale ~10 h, we do not try to account for the distribution of water among different sizes and types of particles. We will be satisfied with a knowledge of the bulk liquid water mixing ratio on a time scale ~10 h. For these purposes, the equations for predicting the hydrometeor mixing

ratios (5.7) can be simplified to the point of considering only one category, namely the total liquid water, represented by mixing ratio q_L. In this case,

$$\bar{q}_i \equiv \bar{q}_L \tag{5.8}$$

The major assumption required to make this simplification is that the rate of fallout, which depends on drop size, can be parameterized. This is accomplished by assuming that the convergence of fallout of water can be expressed as

$$F = \frac{\partial}{\partial z}\left(\hat{V}\bar{q}_L\right) \tag{5.9}$$

where $\hat{V}$ is the mass-weighted average particle fall speed, as defined in (3.69). The expression in (5.9) is like that in (3.75), except that the falling drops are not considered to be large raindrops, but rather slowly settling cloud or drizzle (Sec. 3.1.3) particles. The size spectrum $N(D)$ of such drops can be measured and substituted into (3.69) to obtain an empirical value of $\hat{V}$. Similarly the measured $N(D)$ may be substituted into an integral like that on the right-hand side of (4.9) to obtain a value of q_L. Repeated measurements of $N(D)$ can be used to obtain a correlation between $\hat{V}$ and q_L. A commonly used formula obtained in this way[116] is

$$\hat{V} = \tilde{a}_3 q_L \tag{5.10}$$

where $\tilde{a}_3 = 6.25$, q_L is in g kg^{-1}, and $\hat{V}$ is in cm s^{-1}.

Since we have only one category of condensed water q_L, the hydrometeor equation (5.7) reduces to a single equation in which the microphysical source terms are C and F. Thus, with substitution from (5.9) and (5.10), (5.7) becomes

$$\frac{\partial \bar{q}_L}{\partial t} = C + \frac{\partial}{\partial z}\left(\tilde{a}_3 \bar{q}_L^2\right) - \frac{\partial}{\partial z}\left(K_L \frac{\partial \bar{q}_L}{\partial z}\right) \tag{5.11}$$

where K_L is the mixing coefficient for liquid water.

Calculating the behavior of fog on the 10-h time scale is critically dependent on accurate calculation of the surface temperature and humidity. We must have

$$\bar{T} = \mathcal{T}_s \quad \text{and} \quad \bar{q}_v = \mathfrak{q}_s \quad \text{at } z = 0 \tag{5.12}$$

where $\mathcal{T}_s$ and $\mathfrak{q}_s$ are the temperature and vapor-mixing ratio of the soil at the earth–air interface, respectively. A traditional but somewhat oversimplified way to treat an underlying soil is by invoking the simple diffusion equation

$$\rho_s c_s \frac{\partial \mathcal{T}_s}{\partial t} = -\frac{\partial}{\partial z}\left(\kappa_s \frac{\partial \mathcal{T}_s}{\partial z}\right) \tag{5.13}$$

where ρ_s, c_s, and κ_s are the density, specific heat at constant pressure, and thermal conductivity of the soil, respectively. At the interface, the following

---

[116] Suggested by Brown and Roach (1976).

balance is assumed:

$$0 = \rho c_p \overline{\Pi} \mathcal{R} - \rho c_p K_\theta \frac{\partial \overline{\theta}}{\partial z} + \kappa_s \frac{\partial \mathcal{T}_s}{\partial z} - \rho L K_v \frac{\partial \overline{q}_v}{\partial z} \tag{5.14}$$

The humidity at the soil surface is estimated according to a parameterization such as the following:[117]

$$\overline{q}_v = M_{ev} \, \overline{q}_{vs} + (1 - M_{ev}) \overline{q}_v \Big|_{(z \, = \, \varepsilon)} \tag{5.15}$$

where q_{vs} is the saturation mixing ratio and M_{ev}, the "efficiency factor for evaporation," is a specified parameter, which ranges from 0 for a dried-out soil to 1 for conditions of saturated soil or dew, and ε is some small distance (e.g., 1 cm).

The physical balance assumed by (5.14) is that the diffusion of sensible heat through the soil exactly balances the net radiative flux plus turbulent eddy fluxes of sensible and latent heat through the air. The flux of moisture within the soil is ignored. To include this flux, a more explicit treatment of the soil moisture and thermodynamics is required. Such a treatment can be implemented, but it is very complex. It gives results that differ moderately in magnitude from the simpler model. In the more explicit case, fluxes of both vapor and liquid water within the soil are calculated along with the thermal diffusion. A soil "system" is envisioned as consisting of four elements: a "soil matrix," dry air, water vapor, and liquid water.[118] The "porosity" of the soil is assumed, that is, the fraction of a given volume of the soil system occupied by the soil matrix. The First Law of Thermodynamics applied to the soil system, together with expressions of mass continuity for each of the four elements of the soil system, leads to coupled prognostic equations for the temperature and liquid water content of the soil. These equations are complex and not sufficiently instructive to repeat here. The interface conditions in the case of the explicit soil system are

$$0 = \rho c_p \overline{\Pi} \mathcal{R} - \rho c_p K_\theta \frac{\partial \overline{\theta}}{\partial z} + \kappa_s \frac{\partial \mathcal{T}_s}{\partial z} + \left(-\rho K_v \frac{\partial \overline{q}_v}{\partial z} - J_v \right) (L_v - \psi_s) \tag{5.16}$$

and

$$0 = -J_v - J_w - \rho K_v \frac{\partial \overline{q}_v}{\partial z} \tag{5.17}$$

where J_v and J_w are the fluxes of water vapor and liquid water in the soil, respectively, and ψ_s is the "soil moisture potential."[119] Equation (5.16) states that the diffusion of sensible heat *and* latent heat through the soil exactly balances the net radiative flux plus turbulent eddy fluxes of sensible and latent heat through the air.

---

[117] See Atwater (1972) as cited in Sievers *et al.* (1983).

[118] See Sievers *et al.* (1983), Forkel *et al.* (1984), and Welch *et al.* (1986) for detailed discussions of this problem.

[119] The soil moisture potential is defined as the difference between the chemical potential of the soil water and free water. It arises because absorption and surface tension (van der Waals forces) are not negligible in the soil water. See Sievers *et al.* (1983).
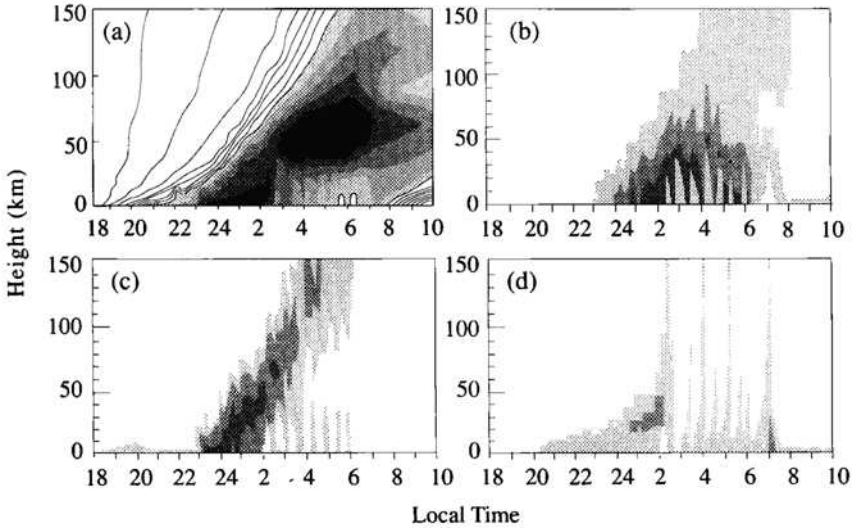
Figure 5.3 Calculated radiation fog development as a function of local time. (a) Temperature contours are at 0.48°C intervals. The colder air is indicated by shading. The lightest shading begins at a threshold of 8.7°C. The darkest shading has a threshold of 6.3°C. (b) Liquid water content (threshold values of 0, 0.15, 0.25 and 0.35 g m^{-3}). In some places the gradient is too tight for all the contours to be seen. (c) Diabatic heating rate (thresholds -1, -2, and -3°C h^{-1}). (d) Mixing coefficient (thresholds 0.001 and 1 m^2 s^{-1}). (Adapted from Welch *et al.*, 1986. Reproduced with permission from the American Meteorological Society.)

Because the latent heat transfer in the soil is now included, the additional equation (5.17) is required, which states that the diffusion of water vapor and liquid water in the soil is exactly balanced at the interface by the turbulent eddy flux of vapor through the atmosphere.

Dew forms whenever the soil temperature is less than the dew point. The downward flux of liquid from the atmosphere and the upward flux of vapor from the soil contribute to the mass of dew.

The usefulness of the thermodynamic equation (5.4) depends critically on its being coupled to an appropriate radiative transfer model. Since the radiative fluxes are affected by the aerosol particles as well as the drops and gaseous constituents, it is important to know the concentration and nature of the dry aerosol particles. Therefore, one or more additional predictive equations may be required to calculate the concentration of aerosol particles.

An example of radiation fog formation, evolution, and dissipation calculated by a scheme of the type described above is shown in Fig. 5.3. In this calculation,[120] the initial local time (LST) is 1800. The initial temperature at the surface is 14°C,

---

[120] This model calculation was made by Welch *et al.* (1986). In addition to the simulation results summarized here, they present observational information confirming the behavior of the model and discuss the model's sensitivity to the turbulence parameterization. Their paper should be consulted for further details about the initial and boundary conditions and how turbulent mixing coefficients are calculated, radiative transfer is formulated, aerosol concentration is estimated, and soil parameters are assigned.

decreasing to 12°C at a height of 0.1 m. The atmosphere is assumed to be isothermal at 12°C up to a height of 0.5 km, decreasing to 11°C at 1 km and to −3°C at 3 km. Initial soil temperature is assumed to increase to 15.5°C at a depth of −5 cm and then to decrease gradually to 15°C at a depth of −1 m. Relative humidity at the initial time is assumed to be 80% up to a height of 0.5 km, then to decrease linearly to 60% at 3 km. The wind at the top of the domain (3-km altitude) is assumed to be geostrophic and 2 m s^{-1}. Atmospheric aerosol particles activated as a function of relative humidity to form embryo droplets, and appropriate schemes for computing solar and infrared radiation are employed. Explicit equations are used for predicting the soil temperature and liquid water content down to a depth of 1 m below the ground.

From 1800 to 2000 LST in the example, the radiative cooling is seen to produce a temperature inversion rapidly. Thus, the height of the boundary layer drops quickly to near the earth's surface. The geostrophic wind layer, lying just above the boundary layer, thus drops almost to the ground. After 2000 LST, the rate of surface cooling decreases considerably, but the inversion continues to increase in intensity. It begins to rise above the surface as turbulent mixing becomes stronger (as indicated by the increase in exchange coefficient shown in Fig. 5.3d). The increased mixing is related to the intensifying shear across the inversion layer. The mixing in the stable layer shifts some of the surface cooling to higher levels, just below the inversion. By 2300 LST cooling below the inversion layer is sufficiently strong that the fog begins to form (as indicated by the appearance of liquid water in Fig. 5.3b). At this time, the strong effect of the fog on the radiation and thus on the generation of turbulence via cooling aloft is seen as the inversion layer suddenly jumps ~10 m upward (Fig. 5.3a). From 0000 to 0200 LST, the inversion layer continues to rise and the strongest cooling begins to occur at the top of the fog layer, rather than at the surface (Fig. 5.3c). As the inversion layer continues to rise, the turbulence continues to increase as the eddies are freer to move about in the deepening boundary layer. The turbulence continues to transfer heat downward, and by just after 0200 LST the minimum temperature lifts off the ground to a position just below the inversion layer bounding the top of the fog. This point in time marks the beginning of a series of oscillations in the fog, which are probably the model's attempt to produce a convective mixed layer in response to the radiative cooling at the top of the fog layer. The net effect of the mixing is to bring liquid water up to higher levels, and the fog layer deepens through the night. Just after 0600 LST, the upper portion of the fog decouples from the lower portion and the oscillations cease. The upper part thus becomes a stratus layer, and only a weak layer of fog is left below. As we will see in the next subsection, it is typical for this layering to occur in fog and stratus in the stable boundary layer. Greenhouse warming below the base of the upper stratus is apparently too great to allow condensation in the layer between the stratus and the weaker fog below. At sunrise, the fog layer dissipates to a thin ground fog, which, after 0750 LST, somewhat surprisingly increases in depth, as dew and soil moisture are evaporated. After 1030, as the insolation intensifies, only high relative humidity and haze persist.

gence of the turbulent flux under stable and unstable conditions, respectively. As the warm air moves over the ice, the boundary layer is rapidly cooled by contact with the surface, and turbulent mixing rapidly spreads the cooling upward. In slightly more than a day's time, the diffusive cooling together with infrared cooling leads to condensation. Once the cloud forms, the radiative regime is greatly altered by the absorptive properties of the droplets. The upper, more dense cloud layer becomes unstable by long-wave loss from the top of the cloud, and a radiative–convective balance is established in the upper cloud layer. Convective warming is approximately equal to radiative cooling at the top, while the convective cooling balances the heating by solar absorption in the interior. The upper cloud retains this character as the steady-state configuration is approached toward the end of the week. The lower, more tenuous cloud layer is characterized by a general balance between the solar heating penetrating into it from above and the diffusive cooling from below. The clear layer separating the upper and lower clouds is in a state of purely radiative equilibrium. Intense heating produced by a greenhouse mechanism precludes condensation in this layer.[122] Another such radiative equilibrium layer exists just below the base of the lower cloud.

The fact that no fog occurs just above the surface during the first hour is a feature of the turbulence parameterization used. When a different, weaker eddy mixing was adopted, the result in Fig. 5.7 was obtained. In this case, fog formed first at the surface and then lifted, as in the case of radiation fog (Fig. 5.3). In this case the steady state is reached and maintained since there is no diurnal cycle to terminate the cloud by the sun rising higher in the sky. When no turbulent fluxes were allowed at all, the lower cloud layer never left the surface, but the cloud nonetheless split into two layers after 3.5 days. These results suggest that in the Arctic, generally persistent layered stratus should prevail, with fog occasionally appearing when the mixing is especially weak. This inference from the calculations is borne out by experience. For example, observers aboard a drifting ice station in the Arctic Basin during the International Geophysical Year observed sky coverage to be over eight-tenths on average throughout the summer months of 1957 and 1958 (Fig. 5.8). These clouds have been described by Professor N. Untersteiner, who was present on the ice station for 366 days, as almost continuously present low stratus, of a "boring" character, interrupted only occasionally by breaks in the cloud cover and occasional periods of fog.

5.2 Stratus, Stratocumulus, and Small Cumulus in a Boundary Layer Heated from Below

5.2.1 General Considerations

Satellite pictures show that great sheets of stratus and stratocumulus are almost always present over the oceans at subtropical latitudes to the west of continents in

---

[122] See Appendix B of Herman and Goody (1976) for a theoretical treatment of the greenhouse mechanism.

the continents. The extent of these regions of oceanic low clouds is so great that it has been estimated that "a mere 4% increase in the area of the globe covered by low-level stratus clouds would be sufficient to offset the 2–3 K predicted rise in global temperature due to a doubling of CO_2."[123]

5.2.2 Cloud-Topped Mixed Layer

5.2.2.1 Conceptual Models

A conceptual model of the development of a cloud-topped mixed layer is given in Fig. 5.10. We will refer to this illustration throughout the following discussion. Panel (a) of the figure represents the boundary-layer structure before any cloud appears. The boundary layer is envisioned to be characterized by a population of buoyant plumes rising from the warm sea surface. It becomes well mixed as a result of the vigorous upward fluxes of sensible and latent heat. Unlike a radiation fog layer, in which buoyancy is suppressed by thermodynamic stability, turbulent kinetic energy is generated strongly by the buoyancy [term $\mathscr{B}$ in (2.86)], as well as by wind shear. The mixing maintains a layer of constant mean equivalent potential temperature $\bar{\theta}_e$ in a layer of depth h. This *mixed layer* is bounded above by a layer of distinctly different $\bar{\theta}_e$, usually higher. The $\bar{\theta}_e$ of the layer aloft is typically maintained by large-scale subsidence in the lower troposphere. In the case of subtropical and tropical oceanic stratus and stratocumulus, the subsidence is associated with the descending branch of the Hadley cell, concentrated in the eastern sectors of the subtropical oceanic anticyclones. In the case of cloud layers in polar airstreams off continents in winter, the subsidence occurs in the cold-air mass behind a front. The change of $\bar{\theta}_e$ across h is represented by $\Delta\theta_e$.[124] The higher $\bar{\theta}_e$ air in the upper layer is entrained by turbulence into the lower layer, thus diluting the boundary layer but at the same time increasing its depth h.

As the depth of the boundary layer increases, the tops of the turbulent elements rise above the lifting condensation level, and small cloud elements form (Fig. 5.10b). As the cloud elements gradually thicken to form a more continuous sheet of cloud at the top of the mixed layer (Fig. 5.10c), the physical picture changes significantly, with radiation taking on an important role. The ocean surface is shielded by the cloud layer and the turbulent heat flux in the subcloud layer becomes weak, or even negative. The turbulent energy generation is concentrated in the cloud layer and is produced by buoyancy as radiative cooling at cloud top destabilizes the layer of cloud. Turbulence is also generated by wind shear in the layer [term $\mathscr{C}$ in (2.86)]. The turbulent layer continues to increase in depth as a result of entrainment.

Finally, the cloud layer breaks up. Observations indicate that when the boundary layer is not extremely unstable, the cloud layer breaks up into stratocumulus

---

[123] This estimate was made by Randall *et al.* (1984).

[124] In this discussion Δ indicates the difference obtained by subtracting the lower-layer value from the upper-layer value.
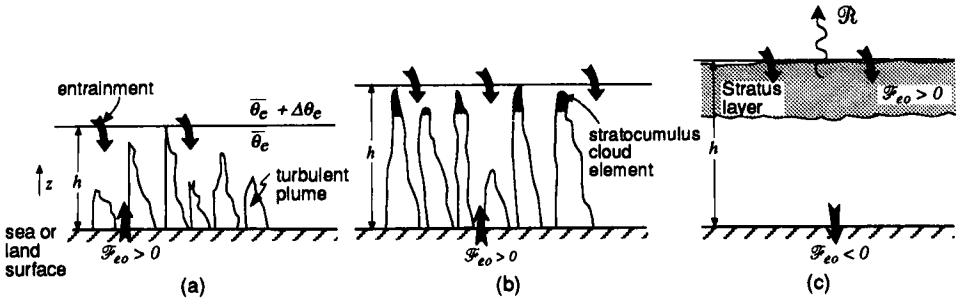
Figure 5.10 Conceptual model of the evolution of a cloud-topped mixed layer over the ocean. (a) Unsaturated turbulent plumes are occurring in a well-mixed layer of depth h. $\mathscr{F}_{eo}$ is the heat flux across the ocean surface. $\bar{\theta}_e$ is the mean equivalent potential temperature in the mixed layer. (b) Plumes reaching above the lifting condensation level have stratocumulus elements in their upper portion. Large arrows indicate entrainment across the top of the mixed layer. (c) Cloud layer becomes solid. Infrared radiative flux $\mathscr{R}$ becomes important, especially at cloud top.
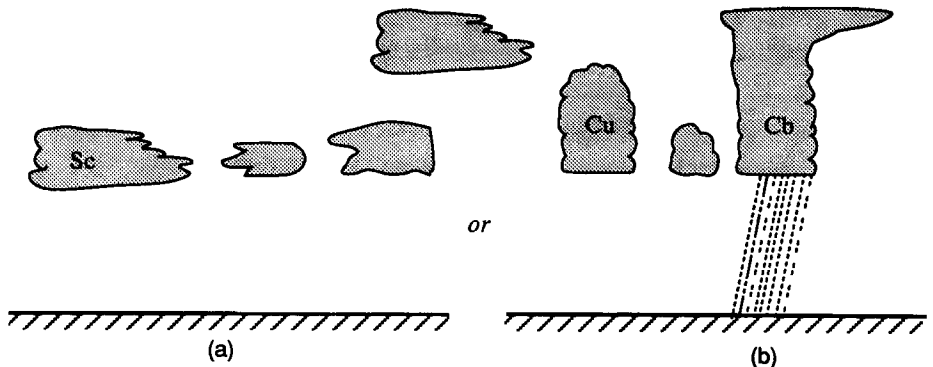
Figure 5.11 Breakup of cloud-topped mixed layer into (a) stratocumulus (Sc) elements and (b) cumulus (Cu) and cumulonimbus (Cb) elements.
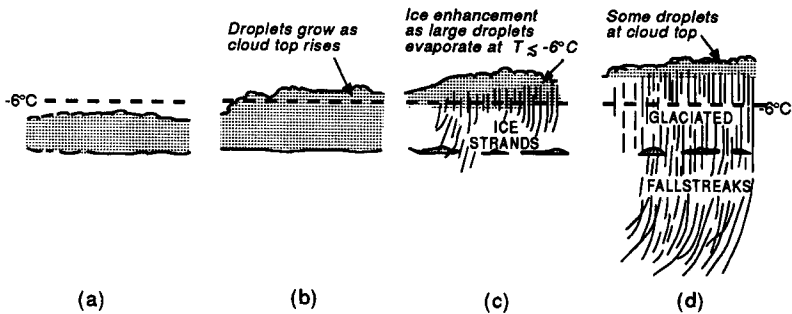

Figure 5.12 Empirical model of the formation of ice in stratocumulus clouds. The model is based on extensive probing of clouds by research aircraft. (From Hobbs and Rangno, 1985. Reprinted with permission from the American Meteorological Society.)

or small cumulus elements, as suggested by Fig. 5.11a. However, when the boundary layer is especially unstable, the elements in the breakup phase may take the form of larger cumulus or even small cumulonimbus (Fig. 5.11b).

The mechanism of the breakup process is not well understood. It has been suggested that it is related to increased entrainment across the top of the mixed layer. The entrainment might be expected to become large and run out of control when the $\Delta\theta_e$ between the boundary layer and the layer above is negative and exceeds a certain large magnitude. According to this idea, a parcel of air entrained into the mixed layer from above, upon mixing with the cloudy air, would become denser than its surroundings. Because of the negative buoyancy, the air from aloft would be rapidly mixed through a portion of the cloud, leaving patchy, dissipating stratocumulus. Observational studies show, however, that the cloud layer persists even when the $\Delta\theta_e$ would appear to be sufficiently negative for instability. The problem appears to be that the potential energy expended in pulling down a tongue of stable air from above exceeds the energy released in the mixing.[125] The cloud-layer breakup problem will be discussed further in Sec. 5.2.3.

When the tops of mixed-layer stratocumulus elements extend to heights above the $-6°C$ level, they sometimes produce high concentrations of ice particles by rapid ice enhancement (Sec. 3.2.6). When the drop size spectrum in the cloud is broad, with largest particles $\sim20\ \mu m$ in dimension, high concentrations of ice are observed to form in ~10 min. These particles fall out in the form of ice strands in the cloud (Fig. 5.12). It has been argued that the most likely ice enhancement mechanism near cloud top is contact nucleation [mechanism (iii) in Sec. 3.2.6].[126] Once the droplets are frozen, they grow by vapor diffusion, while smaller super-cooled droplets in their vicinity evaporate or are collected by the growing ice particles. Thus, the cloud element is rapidly glaciated. Aircraft observations show that the strands of ice particles extend down through the cloud, rapidly removing the liquid cloud particles. Finally, all that remain are a few remnants of the original cloud and streamers of falling ice particles extending below the original cloud base.

5.2.2.2 Mathematical Modeling

The essential dynamics of the development of the cloud atop the mixed layer (depicted schematically in Fig. 5.10a–c) can be examined quantitatively through a consideration of the thermodynamic and water-continuity equations integrated over the depth h of the boundary layer.[127] For simplicity, we will consider the cloud to be warm (no ice) and nonprecipitating, although in reality drizzle may sometimes form and contribute significantly to the water budget of the stratus

---

[125] For a discussion of this problem, see Siems *et al.* (1990).

[126] See Hobbs and Rangno (1985) for details of the argument.

[127] The treatment of the cloud-topped boundary layer presented here was introduced in a seminal paper by Lilly (1968).

5.3   Cirriform Clouds

5.3.1   General Considerations

5.3.1.1   Descriptive Terminology

As we saw in Sec. 1.2.4, upper-tropospheric clouds that exist at temperatures of about −20 to −85°C are referred to as cirrus, cirrostratus, and cirrocumulus. The various forms taken by these clouds, as seen by an observer on the ground, were shown in Figs. 1.15–1.17. In addition to these forms, the tops of deep precipitating cloud systems seen by satellite (Figs. 1.27–1.30) typically occur at these high altitudes. Strong wind shear aloft can displace these upper cloud layers, producing long streamers of high cloud extending great distances downshear from the parent phenomenon. These streamers of cloud are extensive partly because ice particles, with their low-saturation vapor pressure, are slow to sublimate and partly because they are not necessarily inactive debris of the parent phenomena, but rather can be continually regenerated by their own cloud dynamics (see Secs. 5.2.2–5.2.4). Henceforth, we will refer to all high-level clouds as *cirriform clouds*, whether they occur atop a major precipitating cloud system or as separate cloud entities.

5.3.1.2   Microphysical, Kinematic, and Radiative Characteristics

Cirriform clouds consist primarily of ice particles, although some embedded convective elements may contain supercooled water for a few minutes at a time. Aircraft observations of the composition of cirriform clouds[139] show ice contents in cirriform clouds to be in the range 0.001–0.25 g m^{-3}, with values of 0.01–0.1 g m^{-3} being typical. The sizes of the particles range from 50 to 1000 μm. The most commonly reported crystal habits are columns, bullets, bullet–rosettes, and plates. Aggregates of crystals are also seen in cirrus.[140] The vertical air motions in cirriform clouds are typically 0.1–0.2 m s^{-1}, except in floccus and uncinus elements, where the vertical velocity is ~1–2 m s^{-1}.[141]

As in fog and stratus, radiation interacts strongly with the dynamics of cirriform clouds. The radiation is, however, more complicated than in fog and stratus because the particles are complex, do not scatter isotropically, and are often present in very low concentrations. A detailed treatment of the radiative transfer in cirriform cloud is beyond the scope of this text, and extensive treatments of these topics already exist.[142] The radiative transfer equations can be solved under

[139] Summarized in Table 1 of Liou (1986).
[140] See Heymsfield and Knight (1988).
[141] See Heymsfield (1975b, 1977) and Gultepe and Heymsfield (1988).
[142] See, for example, the book by Liou (1980) and the review articles by Stephens (1984) and Liou (1986).

various sets of assumptions. The example results shown in Fig. 5.27 assume that the crystals are columns and use empirical information on optical depth, contribution of scattering to optical depth, and the normalized scattering phase function. With these factors taken into account, the heating of air as a result of the divergence of net radiative flux through cirriform cloud of various depths has been estimated.[143] Heating by solar radiation is felt through the cloud layer, while infrared wavelengths produce a destabilizing effect by cooling the cloud top and warming the base of the cloud.

5.3.1.3   Climatology

In any global satellite picture (e.g., frontispiece), many of the photographed cloud tops are cirriform.[144] Climatologies showing the global extent and distribution of cirriform cloud have been constructed from both satellite observations (dashed curve in Fig. 5.28) and visual observations of the state of the sky (solid curve in Fig. 5.28). Both types of climatology indicate maxima of cirriform cloud in the tropics and midlatitudes and minima in the subtropics. These curves tend to mirror the global distribution of precipitation (dotted curve in Fig. 5.28), indicating that most cirriform cloud is of the type that has its origin in the upper layers of deep, precipitating cloud systems.[145]

5.3.1.4   Approach to Studying the Dynamics

A common form of cirriform cloud is a small convective entity described as consisting of a dense *head* and a long fibrous tail (or *fallstreak*) of falling snow. This form is seen in both cirrus uncinus (Fig. 1.15c) and cirrus spissatus with virga (Fig. 1.16). The uncinus or floccus elements may occur either alone or as convective elements embedded in a widespread layer of cirriform cloud. In examining the dynamics of cirriform clouds, we will first examine (in Sec. 5.3.2) the dynamics of the basic uncinus or floccus element.

We have also noted that cirriform cloud comprises the upper portions of deep precipitating cloud systems and that layers of cirriform cloud extend downwind of the deep cloud systems where the upper portion of such a deep cloud spreads into the environment. As an example of this process, we consider in Sec. 5.3.3 the dynamics of the ice-cloud layer produced by a cumulonimbus cloud (such as illustrated in Fig. 1.5).

---

[143] See Liou (1986).

[144] Actually, the area covered by cirriform cloud is even greater than that apparent in satellite images, as much cirriform cloud is too thin to be seen in satellite imagery and is barely evident to the naked eye. The existence of such thin cirriform cloud is indicated by sensitive aircraft instruments and certain ground-based remote-sensing devices.

[145] The high percent cloud cover by cirrus indicated by the visual observation in high latitudes does not contradict this conclusion, since the precipitation totals at high latitudes must be low because of the small surface areas encompassed by high-latitude circles and the low surface temperatures.
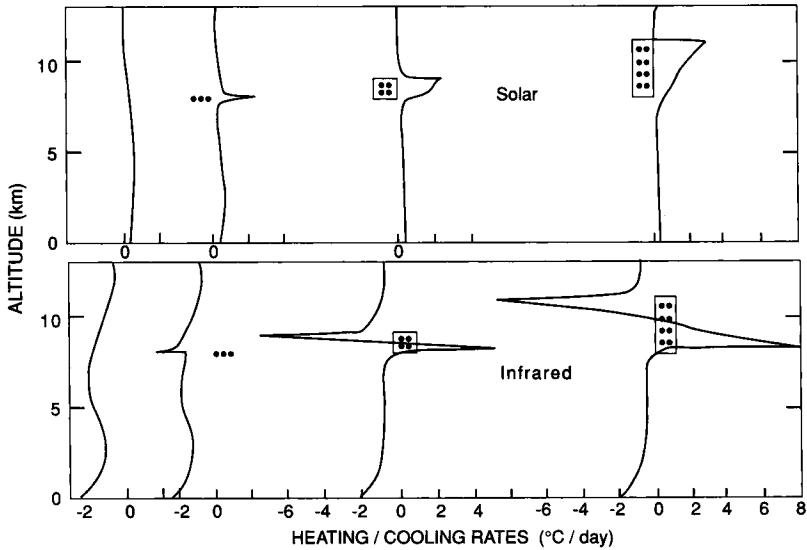
Figure 5.27 Heating of air as a result of the divergence of net radiative flux in atmospheres with cirriform cloud of thicknesses 0, 0.1, 1, and 3 km (dotted boxes). The base of the cirriform cloud is placed at 8 km. Standard atmospheric conditions were assumed. The mean ice content of the cloud layer was 0.13 g m^{-3}, and the cosine of the solar zenith angle was 0.5. Upper panel is for the solar flux. Lower panel is for the infrared. (Adapted from Liou, 1986. Reproduced with permission from the American Meteorological Society.)
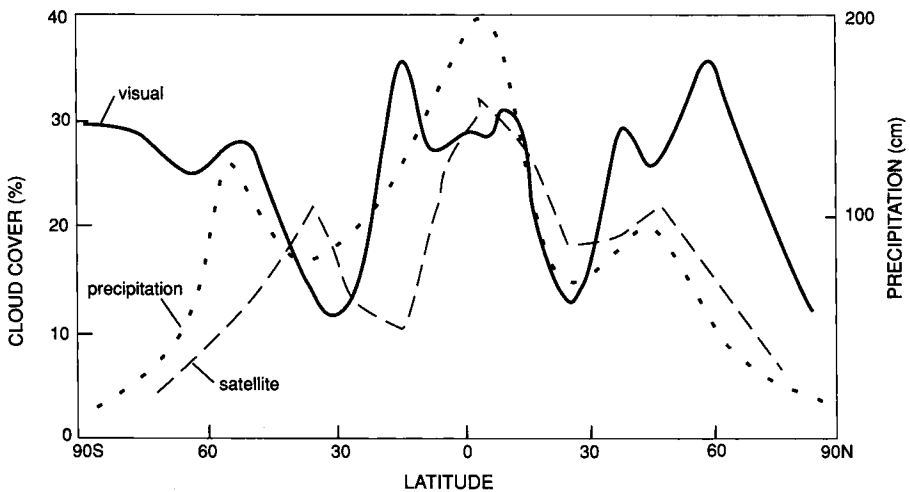
Figure 5.28 Global climatology of cloud cover by cirriform cloud. Visual observations (December, January, February conditions) are from Warren *et al.* (1988). Satellite observations (December, January, February) are from Barton (1983). Global precipitation is from Sellers (1965).

Figure 5.30 Empirical model of a cirrus uncinus element. (a) Wind shear opposite to that in Fig. 5.29. (b) No wind shear. (From Heymsfield, 1975b. Reprinted with permission from the American Meteorological Society.)
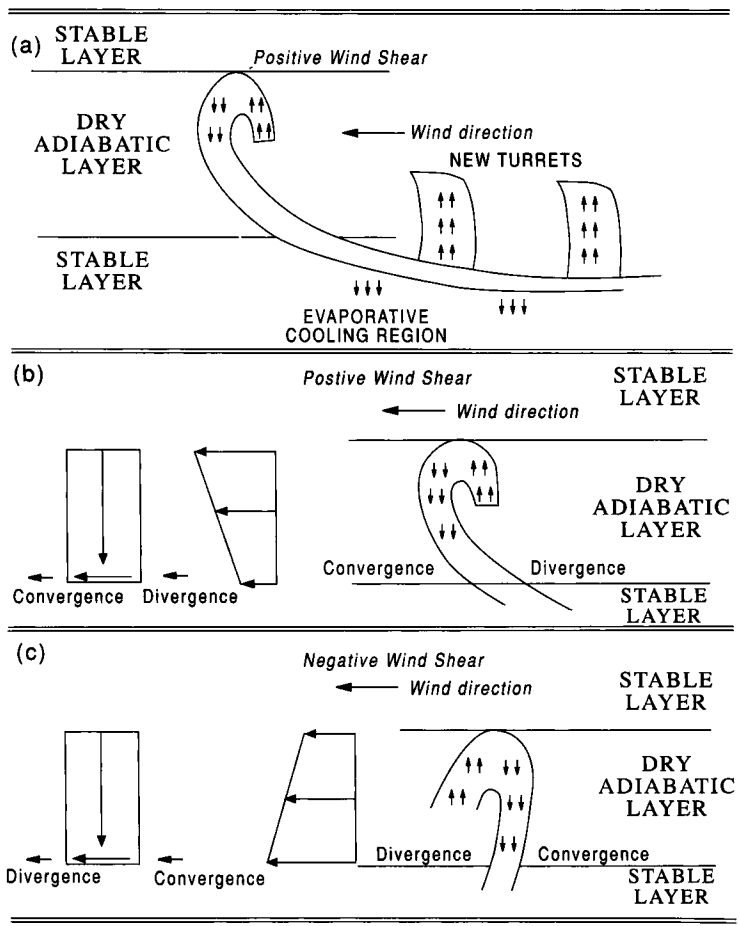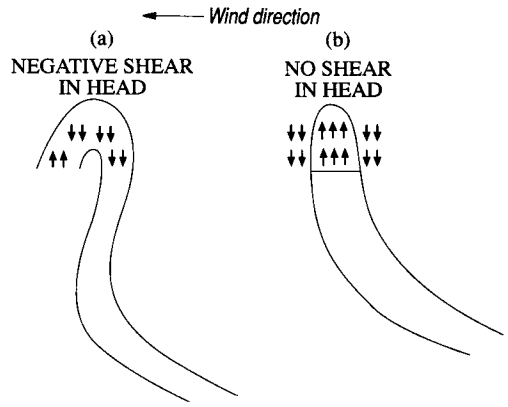

Figure 5.31 How new cirrus uncinus elements may be generated by older elements. (a) Cooling by evaporation causes turbulence in the stable layer, which in turn perturbs the unstable layer above; (b) because of the shear in the environment, horizontal momentum transported downward in the downdraft produces convergence at the bottom of the unstable layer on one side of the downdraft; (c) opposite shear to that in (b) produces shear on the other side of the downdraft. (From Heymsfield, 1975b. Reprinted with permission from the American Meteorological Society.)
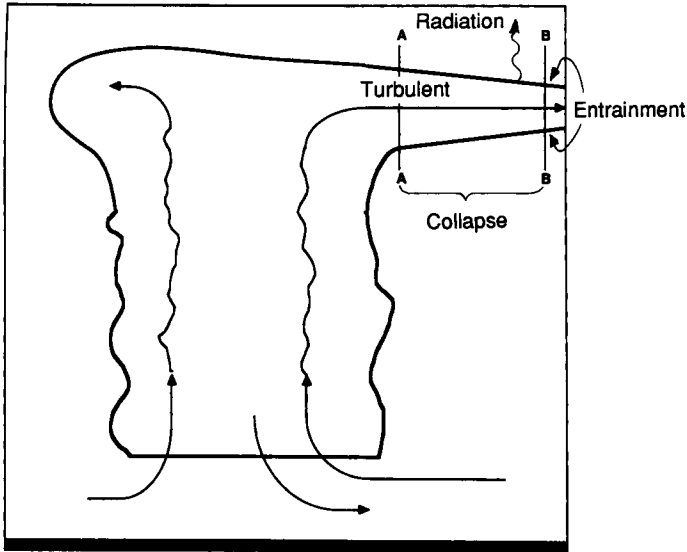
Figure 5.32 Idealized outflow of cirriform cloud from cumulonimbus. Vertical lines AA and BB indicate positions of cross sections in Fig. 5.33. (Adapted from Lilly, 1988. Reproduced with permission from the American Meteorological Society.)
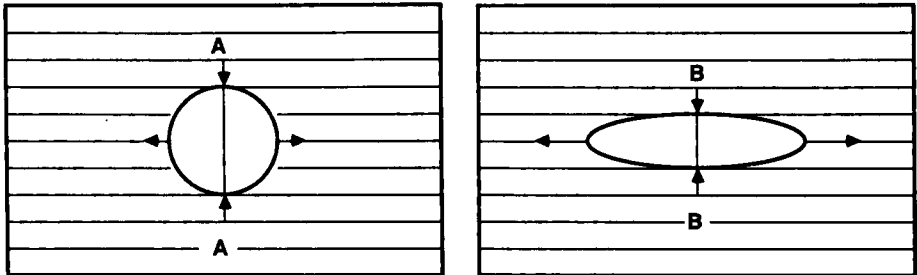

Figure 5.33 Collapse of a cumulonimbus anvil. Plume cross sections are shown for positions AA and BB in Fig. 5.32. The horizontal lines indicate potential temperature surfaces in the environment; the arrows indicate the motion field induced by the buoyancy difference between the outflow plume and the environment. (From Lilly, 1988. Reprinted with permission from the American Meteorological Society.)

slowly dissipated, its energy being transferred to waves and larger-scale two-dimensional turbulence.[148]

In the second stage of development of the outflow plume, the radiative destabilization of the outflow layer becomes important, and the ice cloud is maintained by a process similar to that of low-level mixed-layer stratus. The energy to maintain

[148] Lilly (1988) considered the external collapse quantitatively by assuming it consists of the conversion of the available potential energy to the kinetic energy of the spreading motion. In a simplified example, he found the plume radius tripled in just under 10 min and suggested that the maximum aspect ratio is achieved after about 20 min.

the turbulence is provided by radiative destabilization of a layer of cirrus—as is indicated for example by the calculations shown in Fig. 5.27. The major difference from the case of boundary-layer stratus is that the unstable layer is bounded by stable layers both above *and* below.

Radiation is the only significant heat source in the ice-cloud outflow layer since latent heat release is negligible at these altitudes. The problem thus simplifies to that of a dry mixed layer, in which case the mean potential temperature θ is constant with respect to z, and

$$\frac{d\bar{\theta}}{dt} = -\frac{\partial}{\partial z}\left(\overline{w'\theta'} + \mathcal{R}\right) = \text{constant in } z \tag{5.41}$$

which is the same as (5.21), except that the difference between θ_e and θ is now ignored. The radiative flux divergence is assumed to be a linear function

$$\frac{\partial \mathcal{R}}{\partial z} = B_o\left(z - z_m\right) - A_o \tag{5.42}$$

where A_o and B_o are positive constants and z_m is the height of the middle of the cloud layer.[149] Integration from cloud base z_b to cloud top z_t shows that the value of the constant in (5.41) is

$$\frac{d\bar{\theta}}{dt} = A_o - \frac{\left(\overline{w'\theta'}\right)_t - \left(\overline{w'\theta'}\right)_b}{2H} \tag{5.43}$$

where

$$H = \frac{z_t - z_b}{2} \tag{5.44}$$

The values of the fluxes at z_t and z_b are both considered to be determined by the rate of turbulent entrainment across the boundary of the mixed layer. Accordingly, we let the fluxes at the top and bottom of the cloud layer be

$$\left(\overline{w'\theta'}\right)_t = -w_{et}(\Delta\theta)_t \tag{5.45}$$

and

$$\left(\overline{w'\theta'}\right)_b = w_{eb}(\Delta\theta)_b \tag{5.46}$$

respectively, where $(\Delta\theta)_t$ and $(\Delta\theta)_b$ are the change in θ across the top and bottom of the layer and w_{et} and w_{eb} are entrainment velocities across the top and bottom. The changes in θ across the top and bottom of the ice-cloud layer are defined as positive numbers:

$$(\Delta\theta)_b = \bar{\theta} - \theta_{o_b}, \quad z = z_b \tag{5.47}$$

---

[149] Lilly (1988) based this assumption on the calculations of Ackerman *et al.* (1988), who considered radiative transfer theory in the context of cirrus near the equatorial tropopause.

$$(\Delta\theta)_t = -\overline{\theta} + \theta_{o_t}, \quad z = z_t \tag{5.48}$$

The sounding of potential temperature in the environment θ_o, including the specific values θ_{o_t} and θ_{o_b} at the top and bottom of the ice-cloud mixed layer, is assumed to be known.

It is readily seen that the expressions (5.45) and (5.46) are analogous to (5.27), which represents the mixing across the top of the boundary layer in the case of stratus and stratocumulus. The ice-cloud layer represented here differs from the boundary-layer cloud, however, in having entrainment across *both* the top and bottom of the cloud layer.

In the case of boundary-layer cloud, the entrainment velocity is inferred from the buoyant production of kinetic energy $\mathcal{B}$ integrated over the depth of the mixed layer. Here we follow a similar procedure, in which (5.40) is simplified to

$$\langle\mathcal{B}\rangle = \frac{g}{\overline{\theta}}\int_{z_b}^{z_t}\overline{w'\theta'}\,dz \tag{5.49}$$

The integral in this expression can be evaluated since $\partial\mathcal{R}/\partial z$ is the known linear function of height (5.42), which, together with the assumption that $(\overline{w'\theta'})_b$ is known, implies that $\overline{w'\theta'}$ is a known quadratic function of z, which is obtained by integrating (5.41) from z_b to z:

$$\overline{w'\theta'} = (\overline{w'\theta'})_b - \frac{d\overline{\theta}}{dt}(z - z_b) - \int_{z_b}^{z}\frac{\partial\mathcal{R}}{\partial z}\,dz$$

$$= (\overline{w'\theta'})_b + (z - z_b)\left[\frac{B_o}{2}(z_t - z) + A_o - \frac{d\overline{\theta}}{dt}\right] \tag{5.50}$$

When this expression is substituted into (5.49), we obtain

$$\langle\mathcal{B}\rangle = \frac{g2H}{\overline{\theta}}\left[(\overline{w'\theta'})_b + H\left(A_o - \frac{d\overline{\theta}}{dt}\right) + \frac{B_oH^2}{3}\right] \tag{5.51}$$

To complete the mathematical description of the ice-cloud layer, some assumption must be made to relate the net buoyancy generation of kinetic energy $\langle\mathcal{B}\rangle$ to the entrainment velocities at the top and bottom of the cloud layer. Just as in the case of the stratus-topped mixed layer, the entrainment velocity at the top of the mixed layer must be related to $\langle\mathcal{B}\rangle$ [as discussed in relation to Eq. (5.40)]. To establish a relationship for the ice-cloud outflow layer, the buoyancy generation of kinetic energy given by (5.49) is subdivided into positive and negative contributions

$$\langle\mathcal{B}\rangle = \langle\mathcal{G}\rangle - \langle\mathcal{N}\rangle \tag{5.52}$$

where

$$\langle \mathcal{G} \rangle = +\frac{g}{\bar{\theta}} \int_{z_b}^{z_t} \left(\overline{w'\theta'}\right)_{\mathcal{G}} dz \tag{5.53}$$

and

$$\langle \mathcal{N} \rangle = -\frac{g}{\bar{\theta}} \int_{z_b}^{z_t} \left(\overline{w'\theta'}\right)_{\mathcal{N}} dz \tag{5.54}$$

Symbol $\mathcal{G}$ indicates generation of eddy kinetic energy [$(\overline{w'\theta'}) > 0$] while $\mathcal{N}$ indicates consumption (i.e., negative generation) of eddy kinetic energy [$(\overline{w'\theta'}) < 0$].

This decomposition is an approach sometimes used in considering a dry (non-cloud-topped) mixed layer just above the ground. The negative fluxes are associated with entrainment and are envisaged as being most strongly felt at the top of the mixed layer, across which all the engulfed plumes must pass, while near the surface only a slight effect is felt since only the most penetrative plumes reach down to these levels (Fig. 5.34a). It is typically assumed that $(\overline{w'\theta'})_{\mathcal{G}}$ and $(\overline{w'\theta'})_{\mathcal{N}}$ both vary linearly, with $(\overline{w'\theta'})_{\mathcal{G}}$ decreasing from $\overline{w'\theta'}$ at the bottom of the layer to zero at the top and $(\overline{w'\theta'})_{\mathcal{N}}$ decreasing from 0 at the bottom to $\overline{w'\theta'}$ at the top (Fig. 5.34b). The net flux then decreases linearly from a positive value at the surface to a negative value at the top of the turbulent layer (Fig. 5.34c).

The procedure followed for the case of ice-cloud outflow is an extension of this dry mixed-layer problem. The effect of the cloud-*top* entrainment (w_{et}) is assumed to decrease linearly to zero at cloud base while the effect of the cloud-*base* entrainment (w_{eb}) is assumed to decrease linearly to zero at cloud top (Fig. 5.35). Then

$$\langle \mathcal{N} \rangle = -\frac{g}{\bar{\theta}} \int_{z_b}^{z_t} \left(\overline{w'\theta'}\right)_{\mathcal{N}} dz = -\frac{gH}{\bar{\theta}} \left[\left(\overline{w'\theta'}\right)_b + \left(\overline{w'\theta'}\right)_t\right] \tag{5.55}$$

In the case of the dry mixed planetary boundary layer, it is assumed that

$$\langle \mathcal{B} \rangle = a\langle \mathcal{G} \rangle \tag{5.56}$$

where a is a positive constant.[150] Extending this assumption to the ice-cloud outflow layer, we can combine (5.43), (5.51), (5.52), (5.55), and (5.56) to obtain

$$\left(\overline{w'\theta'}\right)_b + \left(\overline{w'\theta'}\right)_t = \frac{(a-1)2H^2 B_o}{3} \tag{5.57}$$

and

$$\langle \mathcal{B} \rangle = \frac{2aB_o H^3 g}{3\bar{\theta}} \tag{5.58}$$

[150] This approach is attributed to Stage and Businger (1981a,b), who based it on empirical studies of the dry boundary layer. Lilly (1988) used a value of $a = 0.8$ for the cumulonimbus outflow calculation.
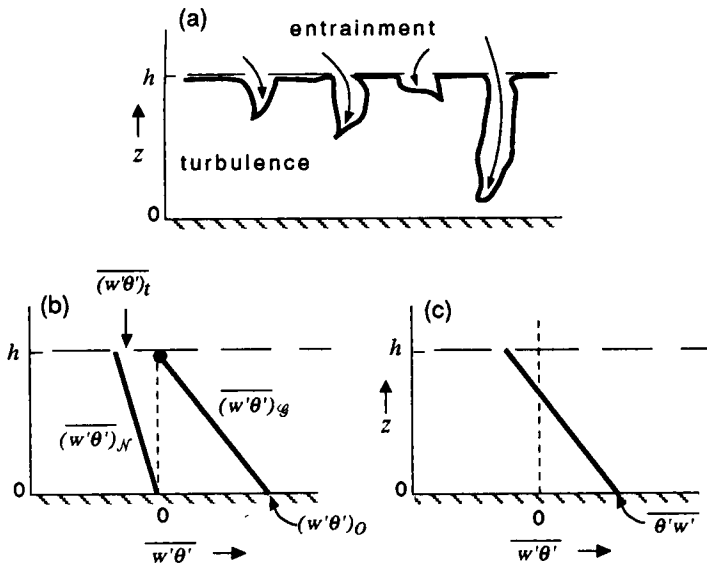
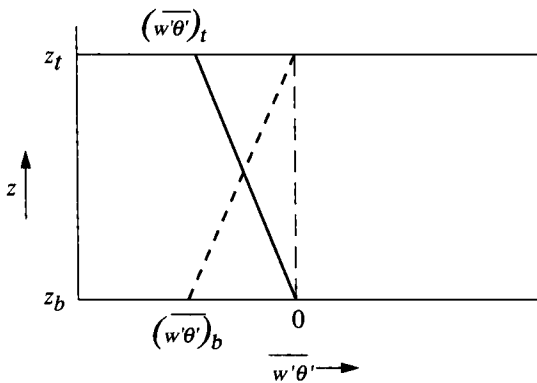**Figure 5.34**   Schematic of a dry (non-cloud-topped) mixed layer just above the ground.

Figure 5.35   Eddy fluxes associated with cloud-top entrainment and cloud-base entrainment in ice-cloud outflow from cumulonimbus. The flux associated with cloud-top entrainment is assumed to have a maximum magnitude $(\overline{w'\theta'})_t$ at z_t and decrease to zero at z_b. The flux associated with cloud-top entrainment is assumed to have a maximum magnitude $(\overline{w'\theta'})_b$ at z_b and decrease to zero at z_t.

which show that the sum of the boundary entrainment fluxes $[(\overline{w'\theta'})_b + (\overline{w'\theta'})_t]$ and the net integrated average eddy heat flux $\langle \mathscr{B} \rangle$ are both driven by the vertical gradient of radiative heating (B_o) in the ice-cloud layer.

Since (5.57) gives only the sum of the values of the boundary fluxes, a way is needed to relate $(\overline{w'\theta'})_b$ and $(\overline{w'\theta'})_t$ in order to close the problem. For simplicity, the two fluxes are arbitrarily made proportional to each other, such that

$$\left(\overline{w'\theta'}\right)_b = \alpha_o\left[\left(\overline{w'\theta'}\right)_b + \left(\overline{w'\theta'}\right)_t\right] \tag{5.59}$$

where α_o is simply an adjustable parameter. Then (5.43) with substitution from (5.57) and (5.59) becomes

$$\frac{d\bar{\theta}}{dt} = A_o + \left(1 - 2\alpha_o\right)\left[\frac{(1 - a)B_o H}{3}\right] \tag{5.60}$$

This equation predicts the mean potential temperature in the ice-cloud mixed layer. The parameter A_o represents the net radiative heating, which if positive causes the layer to warm. The jump in θ at the top of the cloud layer decreases, while that at the bottom of the layer increases. The second term is proportional to B_o, which represents the vertical gradient of the radiative heating, which drives the turbulence and entrainment. If the adjustable parameter $\alpha_o > 0.5$, then the temperature rise in the mixed layer is less than that provided by the net radiation because more potentially cool air is entrained at the bottom than warm air at the top of the cloud. The opposite situation applies if $\alpha_o < 0.5$.

Substitution of (5.57) and (5.59) into (5.45) and (5.46) gives

$$\frac{dz_b}{dt} = -\frac{2\alpha_o(1 - a)B_o H^2}{3(\Delta\theta)_b} \tag{5.61}$$

and

$$\frac{dz_t}{dt} = \frac{2(1 - \alpha_o)(1 - a)B_o H^2}{3(\Delta\theta)_t} \tag{5.62}$$

which, together with (5.60), form a closed set of equations for calculating $\bar{\theta}$, z_b, and z_t as functions of time. For values of $A_o = 0$ (no net radiative heating) and $\alpha = 0.5$ (equal effect of entrainment at cloud top and cloud base), the change in the depth of the mixed layer is found to be slow—rather similar to boundary-layer stratus. If α is again 0.5 but $A_o > 0$ (i.e., radiation is warming the cloud layer in the mean), then $\bar{\theta}$ increases until the jump $(\Delta\theta)_t$ at cloud top becomes small. Then, according to (5.62), the rate of increase in the cloud-layer depth becomes large.[151]

5.3.4 Cirriform Cloud in a Thin Layer Apart from a Generating Source

The final type of cirriform cloud we will look at is that which occurs in a thin unstable layer aloft, apart from a generating source such as a cumulonimbus cloud. The dynamics of this type of cirriform cloud have been examined via a numerical model.[152] The model applies in the two-dimensional $(x-z)$ spatial domain indicated in Fig. 5.36. The domain is a shallow layer, in which the two-dimensional Boussinesq vorticity equation (2.61) may be used to describe the air motions, and nothing varies in the y-direction. If turbulent mixing in the layer is

---

[151] See Lilly (1988) for further discussion of these results.
[152] This numerical model is described in a pair of papers by Starr and Cox (1985a,b). The present discussion is based on that work.

Results obtained for a basic-state vertical motion $w_B = 2$ cm s^{-1} are shown in Figs. 5.38–5.40. Most evident in Fig. 5.38 is the strong effect of the fall speed of the crystals that comprise the cloud. With time, the height of the cloud base and the height and amount of the maximum ice concentration decrease substantially, especially during the first 20 min of the lifetime of the ice-cloud layer. Figure 5.39 shows the vertical profiles of heating in the cloud layer associated with latent heat release as well as infrared, solar, and net radiation at three different stages of the lifetime of the cirriform cloud layer. The latent heating by vapor deposition where the cloud has formed and cooling by sublimation of ice below the cloud layer are generally of the same order of magnitude as the radiative heating and cooling. A somewhat surprising result is that the net radiative heating curve indicates little if any destabilization of the cloud layer. These properties of the model of cirriform cloud formation suggest that the assumptions we made in Sec. 5.3.3, which involved viewing a cirriform cloud layer as a radiatively driven mixed layer, may not always be met. In that treatment, the fall speed of the ice particles was tacitly neglected and the profile of heating used was one appropriate for an extremely high layer of cirriform cloud.[153] From Fig. 5.40, it is evident that despite the lack of strong radiative destabilization, embedded cellular structure remains evident throughout the lifetime of the cirriform cloud layer; however, it decreases in intensity in the later stages.

5.4 Altostratus and Altocumulus

5.4.1 Altostratus and Altocumulus Produced as Remnants of Other Clouds

Like high-level cirriform cloud, middle-level altostratus and altocumulus may be produced as remnants of nimbostratus or cumulonimbus. Figure 5.41 is the result of a numerical simulation (using a model of the type to be discussed in Sec. 7.5.3) of a growing tropical cumulonimbus, which can be seen to issue protruding layers of cloud in middle (as well as lower) levels.[154] This behavior is related to the variation of the horizontal wind field in and around the cloud.

5.4.2 Altocumulus as High-Based Convective Clouds

Altostratus and altocumulus may also form in layers aloft, completely removed from any deep nimbostratus or cumulonimbus source. One important type is simply cumulus or cumulonimbus with middle-level bases (i.e., altocumulus cas-

---

[153] The fact that these assumptions may not always be met was recognized and pointed out by Lilly (1988).

[154] That these simulations represent realistic cloud structures over the equatorial Atlantic Ocean was verified by means of stereoscopic cloud photography by Warner *et al.* (1980).
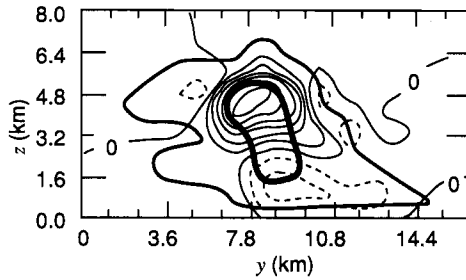
Figure 5.41 Model simulation of a cumulus congestus cloud over the tropical eastern Atlantic Ocean. Cross section runs north–south through a three-dimensional domain. Heavy contours show liquid water content in g m^{-3}. Thin isopleths are for vertical velocity at 1 m s^{-1} intervals; dashed contours are for downdrafts. (From Simpson and van Helvoirt, 1980.)

tellanus, Fig. 1.14d). The dynamics of these cloud elements are well described by the cumulus and cumulonimbus dynamics discussed in Chapters 7 and 8.

5.4.3 Altostratus and Altocumulus as Shallow-Layer Clouds Aloft

Many altostratus and altocumulus clouds are neither the remnants of other clouds nor cumulus or cumulonimbus clouds aloft. These clouds include altostratus layers such as the one seen in Fig. 1.13 and altocumulus stratiformis (Fig. 1.14a and b). These are layer clouds that closely resemble stratus and stratocumulus. However, they do not occur in the planetary boundary layer, and their dynamics are therefore not exactly analogous to those of stratus and stratocumulus (Secs. 5.1 and 5.2). They are more similar to the cirriform cloud layers described in Sec. 5.3 in that they occur in shallow layers of air aloft, separate from the boundary layer.

The dynamics of this type of altostratus and altocumulus can be investigated by means of model calculations like those used in Sec. 5.3.4 to describe a thin layer of cirriform cloud. That model has been modified to middle-level cloud conditions by changing the fall velocity relationship and radiative absorption coefficients to make them appropriate for a cloud of liquid water drops and calculating condensation and evaporation based on 100% relative humidity with respect to liquid wa-

Figure 5.39 Results of model of cirriform cloud formation in a layer of air in which the basic-state vertical motion $w_o = 2$ cm s^{-1}. Vertical profiles of horizontally averaged heating by phase changes of water (QC), infrared radiation (QIR), absorption of solar radiation (QSW), and net radiative processes (QR). (From Starr and Cox, 1985a. Reprinted with permission from the American Meteorological Society.)

Figure 5.40 Results of a model of cirriform cloud formation in a layer of air in which the basic-state vertical motion $w_o = 2$ cm s^{-1}. Ice–water mixing ratio field in μg g^{-1} at various times. Contours for 20 and 40 μg g^{-1} are shown by shading. (From Starr and Cox, 1985a. Reprinted with permission from the American Meteorological Society.)

ter.[155] In calculations illustrated in Fig. 5.42, the fall velocity was assumed to be 0.9 cm s^{-1}—two orders of magnitude less than that assumed in the case of cirriform cloud (~1 m s^{-1}, as in Fig. 5.37). Because of the smaller particle fall speeds, the simulated middle-level cloud retains its hydrometeors throughout the cloud lifetime, has larger mixing ratios of hydrometeor mass, and is contained in a shallower layer than the cirriform cloud (cf. Fig. 5.40 and Fig. 5.42). As in the cirriform cloud layer, the latent heat release and radiative heating are of the same order of magnitude (Fig. 5.43). However, unlike the model cirriform cloud layer, the radiative heating produces destabilization in the middle-level cloud, strongly cooling the upper part of the cloud layer and warming it below. Consequently, turbulent kinetic energy is maintained throughout the cloud lifetime (Fig. 5.44).

[155] This calculation was carried out by Starr and Cox (1985a,b) as part of the same study in which they modeled the thin layer of cirrus. Although this calculation was originally described as representing altostratus, it probably better represents altocumulus stratiformis, since altostratus is often deeper than the cloud assumed in the simulation and is more often than not glaciated while altocumulus stratiformis is shallow, contains overturning convective elements, and tends to consist of supercooled liquid water (at least during its earlier stages).
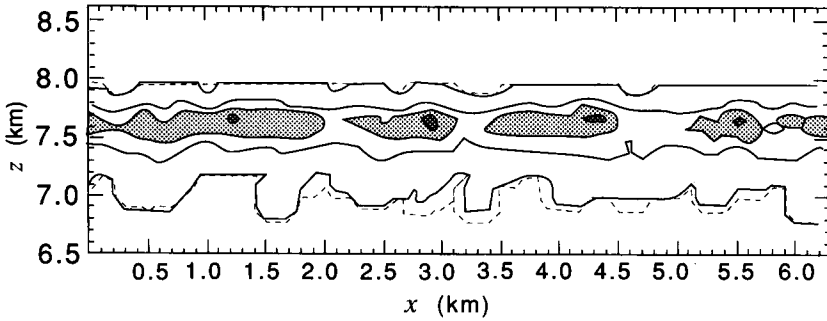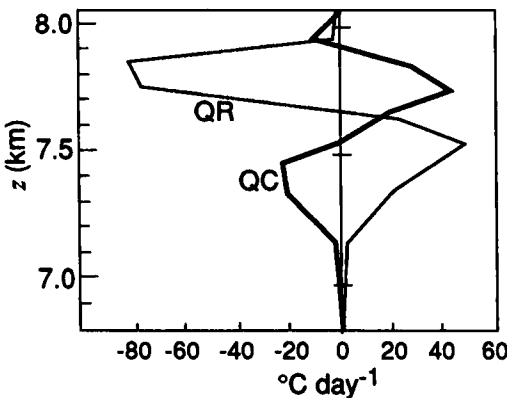

Figure 5.42

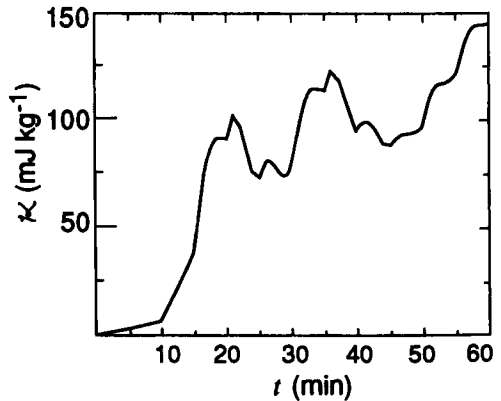
Figure 5.43   **Figure 5.44**

Thus, a middle-level cloud layer (altocumulus stratiformis) could be described appropriately by the theory of a cloud-filled radiatively driven mixed layer aloft, which was used in Sec. 5.3.3 to describe the layer of ice cloud generated by cumulonimbus.

The interpretation of altocumulus stratiformis as a cloud-filled radiatively driven mixed layer helps to explain its structure since the elements of altocumulus stratiformis often appear to be produced by Rayleigh–Bénard convection (as described in Sec. 2.9.3) in the form of cells (Fig. 1.14a) or rolls (Fig. 1.14b). The differential heating mechanism driving the Rayleigh–Bénard convection is evidently the infrared radiation, and the presence or absence of shear likely determines whether or not the elements take the form of rolls (Fig. 5.20). The average distance between altocumulus (and cirrocumulus) rolls has been reported to be <0.25 km in 39% of cases, <0.5 km in 78% of cases, and <0.75 km in 93% of cases.[156] The observed depths of the cloud layers moreover indicated a horizontal-to-vertical aspect ratio ~1:1, which is consistent with the rolls being of the Rayleigh–Bénard type.

In some cases, altocumulus rolls are produced by shear instability, probably of the Kelvin–Helmholtz type (Sec. 2.9.2), or they may be the result of mixed thermal and shear instability. These distinctions can be difficult to make in visual observations of clouds.

5.4.4 Ice Particle Generation by Altocumulus Elements

The individual elements (rolls or cells) of altocumulus stratiformis tend to glaciate and produce fallstreaks of precipitating ice particles in the later stages of their lifetimes (Fig. 5.45). The process appears to be similar to that which occurs in stratocumulus (Fig. 5.12). In their glaciating stage, the elements of altocumulus

---

[156] Data reported by Süring (1941) and discussed further by Borovikov *et al.* (1963). The book of Borovikov *et al.* (1963) is of interest as one of the first attempts at a comprehensive treatment of cloud dynamics.

Figure 5.42 Results of a model of middle-level cloud formation. Nighttime conditions were assumed and the basic-state vertical motion was $w_B = 2$ cm s^{-1}. Liquid–water mixing ratio field in contours of 0.001, 1, 50, 100, and 150 μg g^{-1}. (From Starr and Cox, 1985b. Reprinted with permission from the American Meteorological Society.)

Figure 5.43 Results of a model of middle-level cloud formation. Nighttime conditions were assumed and the basic-state vertical motion was $w_B = 2$ cm s^{-1}. Vertical profiles of horizontally averaged heating by phase changes of water (QC) and infrared radiation (QR). (From Starr and Cox, 1985b. Reprinted with permission from the American Meteorological Society.)

Figure 5.44 Results of a model of middle-level cloud formation. Nighttime conditions were assumed and the basic-state vertical motion was $w_B = 2$ cm s^{-1}. Domain-averaged turbulent kinetic energy as a function of time. (From Starr and Cox, 1985b. Reprinted with permission from the American Meteorological Society.)